

pubs.acs.org/Macromolecules Article

Tuning Solvent Quality Induces Morphological Phase Transitions in Miktoarm Star Polymer Films

Zerihun G. Workineh,* Giuseppe Pellicane,* and Mesfin Tsige*



Cite This: https://dx.doi.org/10.1021/acs.macromol.0c00770



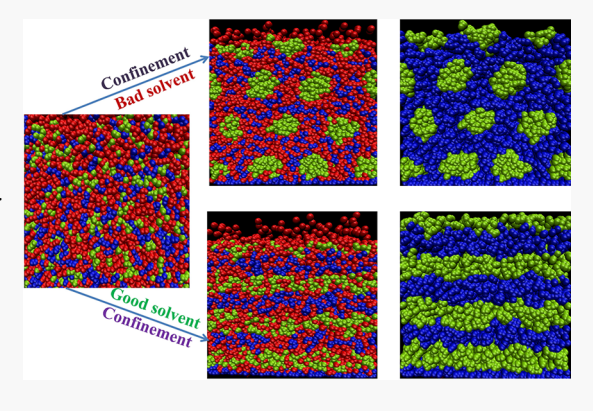
ACCESS

III Metrics & More

Article Recommendations

Supporting Information

ABSTRACT: The ordering and kinetics of self-assembly of miktoarm star polymers of the form $(A_n)_k-C-(B_n)_k$ in solution and confined between two surfaces are investigated using a coarse-grained molecular dynamics simulation, with the ultimate goal of developing predictive capabilities for these systems. By systematically changing the relative solvent-block interaction for one block, combined with the effect of confining substrate on one side and vapor on the other side, we observed a number of interesting morphologies for an inherently lamellar miktoarm star polymers in the absence of solvent. Furthermore, we also found that in solution the self-assembly kinetics of miktoarm star polymers into cylindrical and lamellar morphologies is completely different from the self-assembly kinetics of linear block copolymers. The findings from the present study can be used to tailor the film morphology of miktoarm star polymers, playing a leading role in guiding the experimentalists for designing this class of materials for different types of applications.



■ INTRODUCTION

Supramolecular self-assembly of 3D globular architectures, such as star copolymers, dendrimers, and hyperbranched polymers, offers a novel route for nanostructure synthesis. Nanostructures formed by these materials display a variety of morphologies including spherical, cylindrical, gyroid, and lamellar structures depending on the conditions at which they are exposed. ¹⁻⁶ These structured phases can be used for a range of applications including drug delivery, ⁷⁻¹⁰ water purification technology, ^{11,12} biocatalysis, ^{13,14} imaging, ¹⁵⁻¹⁷ fuel cells, ¹⁸⁻²⁰ nanoelectronics, ²¹ and capacitors. ²²

Miktoarm star polymer, hereafter referred as MSP, is a special type of polymer with at least two distinct types of chains attached to a common center. Due to their novel architectures, MSPs can form nanostructures with emergent physical and chemical properties which are different from the ones exhibited by their linear counterparts. Multicompartment micelles, worm-like micelles, and other interesting structures via the self-assembly of ABC-type miktoarm star-like copolymers have been successfully achieved. Several Janus structures have also been constructed via microphase separation of miktoarm star PS-b-PB-b-PMMA copolymers. Self-assembly driven nanostructures of MSPs have shown to be highly dependent on the arm length and solvent conditions. Significantly affected by the number and length of the arms of MSP. Self-assembly behavior in the bulk can be significantly affected by the number and length of the arms of MSP.

Several experimental, theoretical, and computational simulation studies have shown that linear block copolymer systems,

hereafter referred as linear BCP, exhibit a number of ordered phases depending on solvent quality, chain length, arm number, and other thermodynamic conditions. Hereafter a For instance, it has been shown that linear BCPs form different morphological structures when $\chi N > 10.5$, where χ is the Flory–Huggins interaction parameter between the blocks and N is the total number of monomer beads in a chain. Different morphologies of linear BCP systems can also be achieved by controlling the annealing conditions. Solvent vapor annealing (SVA) and direct immersion annealing (DIA) are some of the annealing techniques that make use of selective solvents and temperature.

Furthermore, confining polymer thin films in a given geometry causes significant deviations of their structural and dynamical properties from their bulk phase behavior. It is experimentally challenging to precisely reveal the in situ morphological evolution of block copolymer films under the combined effect of several parameters. Thus, computational simulations that quantify morphological evolution and explain dependence on numerous parameters are needed.

Received: April 13, 2020 Revised: July 3, 2020



Macromolecules Article pubs.acs.org/Macromolecules

The effect of polymer concentration, solvent quality, and annealing time on the formation of different morphologies have been investigated by several researchers. 58,59 A number of simulation studies of linear BCP thin films under swelling and solvent evaporation condition have been conducted.^{60–62} We have recently shown that the combined effect of confinement and solvent quality on linear block copolymer morphology can be used as a route for controlling the morphology of block copolymer thin films.⁶³ A similar investigation of miktoarm star polymers under confinement and different solvent quality is, however, missing to the best of our knowledge.

The main purpose of this work is to gain a fundamental understanding of the effect of solvent quality and substrate characteristics on final morphology, domain size, and ordering (long- and short-range) in solvent swollen MSP thin films. Furthermore, the results from this simulation study will be compared with our recent results for linear BCP thin films. 63 In the current study, we expect to provide a general framework to understand the structure of MSPs confined in between a flat impenetrable substrate and a solvent vapor by performing extensive molecular dynamics simulations using bead-spring model of MSP thin films. Our goal is to guide the experimentalists in choosing the solvent and substrate combination to obtain desired MSP thin film morphology. The rest of the paper is arranged as follows; section 2 deals with simulation models used and details of our simulation; our simulation results are presented and discussed in section 3 and the conclusion from the present work is given in section 4.

SIMULATION MODEL AND DETAILS

Simulation Model. In this simulation study, a four arm number referred as $(A_n)_2 - C - (B_n)_2$ star polymer has been considered. The central bead (C) and the beads of the two arms (A) are considered as high swelling beads (referred hereafter as HSB or type 3) whereas beads of the other two arms (B) are the low swelling beads (referred hereafter as LSB or type 2) as shown in Figure 1. In order to compare with our previous simulation work of symmetric linear block copolymer of A₂₀B₂₀ in solution, the chain length of each arm in the present study is 10 coarse-grained beads long with 21 HSB beads (including the central bead) and 20 LSB beads. Thus, the total number of beads of the star polymer in the present study is 41. The total number

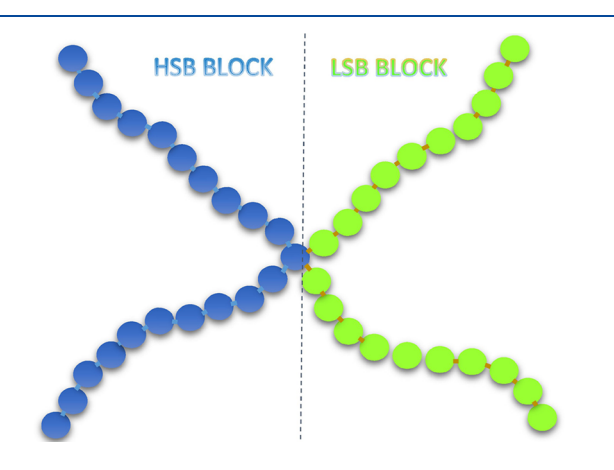


Figure 1. Schematic representation of arm number 4 and arm length 10 MSP with two immiscible distinct blocks (HSB and LSB) of coarsegrained beads. Blue beads and green beads represent HSB and LSB blocks, respectively, throughout the manuscript.

of star polymers taken for this simulation has been 1331, which gives 54 571 total number of beads. The solvent referred hereafter as SOL (or type 1) is modeled as single monomers with a total number of 54872 beads, which corresponds to a swelling ratio of $SR \approx 2$ (defined as the ratio of the number of solvent beads to the number of HSB beads).

FENE potential is used to calculate the bond interactions between bonded beads. Furthermore, interactions between different types of nonbonded beads are calculated by the following 12-6 Lennard-Jones (LJ) potential:

$$U_{\rm LJ}(r_{ij}) = 4\epsilon_{ij} \left[\left(\frac{\sigma_{ij}}{r_{ij}} \right)^{12} - \left(\frac{\sigma_{ij}}{r_{ij}} \right)^{6} \right] - U(r_{\rm c})$$
(1)

where $U(r_c)$ is a constant that guarantees the LJ potential energy is continuous at the cutoff distance of r_c , r_{ij} is the distance between nonbonded beads i and j, ϵ_{ij} is the depth of the potential well, and σ_{ii} is the finite distance between beads at which the interparticle potential is zero and is set to 1 for all cases. Interactions between nonbonded LSB and HSB beads are purely repulsive with the cutoff radius $r_c = 2^{1/6}\sigma$. List of parameters for different cohesive and pairwise interactions between the beads are given in Table 1. The cohesive interaction between HSB beads is taken to be stronger than that of LSB beads, which implies that the surface tension of LSB is smaller than HSB.⁶³-

Table 1. Interaction Parameter (ϵ_{ij}) and Cutoff Radius (r_c) for Different Types of Bead Pairs'

pairs (ij)	ϵ_{ij}	$r_{\rm c}$
SOL-SOL(11)	1.1	2.5
LSB-LSB(22)	0.9	2.5
HSB-HSB(33)	1.0	2.5
LSB-HSB(23)	1.0	1.12
SOL-HSB(13)	1.2	2.5
SOL-SUB (1 sub)	1.0	1.12
LSB-SUB(2 sub)	1.0	1.12
HSB-SUB(3 sub)	10.0	3.5

 ${}^{a}\epsilon_{12}$ was made to vary from 0.75 to 1.10 with an increment of 0.05 keeping the rest of the interaction parameters constant.

The purpose of varying SOL-LSB interaction parameter (ϵ_{12}), while keeping the other interaction parameters fixed, is to study solely the effect of quality of solvent on the morphology of the simulated systems. The interaction potentials of all blocks with the substrate are also modeled by the LJ potential model.⁶³ However, the strength of interactions of different blocks with the substrate varies depending on the wetting preference of the substrate. An $\epsilon=10$ used for the substrate-HSB interaction energy (see Table 1), corresponds to 25-42 kJ/mol^{76,7} implying that there is a strong hydrogen bonding interaction between HSB block and the substrate. Solvent-substrate and LSB-substrate pair interactions are considered to be purely repulsive (see Table 1) to make the substrate strongly selective to the swelling (HSB) block only.

Simulation Details. A detailed description about initial system preparation is given in our previous work.⁶³ For completeness, we have provided the details of the initial film preparation in the Supporting Information (SI). Note that in experiments such as solvent vapor annealing (SVA), 78,79 a block polymer film is exposed to vapors of one or more solvents until it is swollen and a mobile polymer film is formed. The other

approach of swelling a block polymer film is to immerse the film in a solvent mixture bath known as direct immersion annealing (DIA). Both approaches involve diffusion of solvents into the polymer film which, unfortunately, is computationally very expensive to do the same in MD simulation. Because of that, we avoid simulating the initial stage of the diffusion of solvents into the film and instead we focus on understanding the effects of solvent-block interaction and substrate after the film is swollen. Furthermore, in both SVA and DIA experiments, a vapor phase usually forms on top of the swollen block copolymer films and to imitate this experimental condition we have added a 3σ vapor region at the top of our polymer film as described in the SI. As shown in Figure S2 of the SI, the equilibrated solvent density in the vapor phase is almost the same for all cases.

Starting from the final state of film preparation, eight different simulations corresponding to the eight different LSB-SOL interaction parameters, ϵ_{12} , were run in parallel using NVT ensemble. All of the simulations were done using the LAMMPS simulation package. The equations of motion were integrated by using a velocity-Verlet algorithm with a time step of $\Delta t = 0.008\tau$, where $\tau = \sigma \left(\frac{m}{\epsilon}\right)^{1/2}$. Each of the simulations was run for at least $4.8 \times 10^5 \tau$ (or 6×10^7 time steps) at constant temperature $T = 1\epsilon/k_{\rm B}$ using the Langevin thermostat.

■ RESULTS AND DISCUSSION

In this section, the dependence of different properties of simulated MSP systems on the relative solvent-block interactions is discussed. Those properties include kinetics of molecular rearrangement, final morphology and molecular level spatial configuration of chains. Moreover, we also discuss the effect of substrate interaction parameter on selective segregation of blocks throughout the film.

We systematically address the effect of solvent quality through LSB-SOL interaction parameter, ϵ_{12} , on the equilibrated morphology and kinetics of MSP films. To do so, ϵ_{12} has been made to vary from 0.75 (poor solvent condition) to 1.1 (good solvent condition) with an increment of 0.05 keeping the HSB-SOL interaction, ϵ_{13} , constant (see Table 1). Based on Table 1, ϵ_{12} = 0.9 corresponds to neutral (theta) solvent condition for the LSB block. Hereafter, poor solvent condition in general will refer to ϵ_{12} < 0.9 and good solvent condition will refer to ϵ_{12} > 0.9.

The surface tensions of HSB and LSB are different such that LSB has a lower surface tension and is expected to wet the free-side (top) of the film in the absence of solvent. The substrate is modeled to be selective to the HSB block. In the absence of solvent, the difference in surface tension between the two blocks combined with the selectivity of the substrate to the HSB block is expected to result in a lamellar morphology with asymmetric wetting where the LSB block wets the free-side and the HSB block wets the substrate. The strength of the LSB-SOL interaction will affect the wetting behavior of the LSB block on the free-side in addition to significantly changing the morphology of the whole film.

In order to understand the effect of solvent quality on the kinetics and equilibrium film morphology, we first investigated the time evolution of the two extreme cases of LSB-SOL interaction parameter used in the present simulation work, ϵ_{12} = 0.75 (poor solvent) and 1.1 (good solvent), shown in Figure 2. As it can be clearly noticed from the snapshots shown in Figure 2, microphase-separated films evolve as a function of time. While major morphological changes occur quickly during the initial softening stage of the blocks, cylindrical (poor solvent

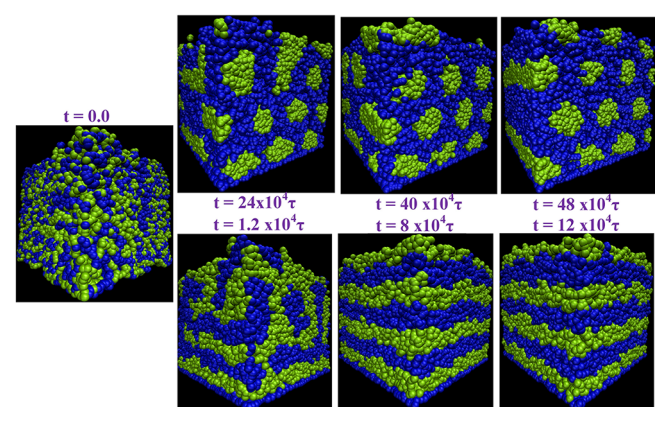


Figure 2. Snapshots showing time evolution of solvent swollen MSP for $\epsilon_{12}=0.75$ (top row) and $\epsilon_{12}=1.1$ (bottom row). Solvent beads are not shown for clarity.

condition) and lamellar (good solvent condition) morphologies are clearly observed at time $t \approx 12 \times 10^4 \tau$ and $48 \times 10^4 \tau$, respectively (see also Figure 4).

To have deeper visual inspection in the region of morphological transition, from cylindrical to lamellar, snapshots containing only LSB blocks as the solvent quality changes from poor to neutral and then to good solvent conditions are shown in Figure 3. The transition seems to be a direct transition from

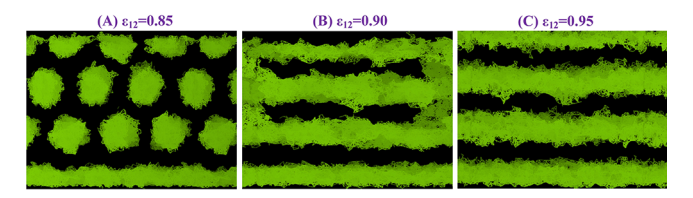


Figure 3. Equilibrated snapshots showing only the LSB blocks in the region of transition from cylindrical to lamellar morphology as solvent quality changes from poor to neutral and then to good solvent conditions.

cylindrical to lamellar morphologies without having frustrated gyroidal intermediate morphological state at neutral solvent condition that was observed in our recent work for linear BCP films. The state at ϵ_{12} = 0.90 (neutral solvent) is in a metastable state since running the simulation much longer than the other cases, $1.2 \times 10^6 \tau$, brought it close to lamellar morphology as shown in Figure 3. As such, the morphology of MSP films, of the type of architecture investigated in the present study, change from cylindrical to lamellar morphology as the quality of solvent for one of the blocks change from poor to good solvent while the solvent is kept as a good solvent for the other block. While solvent induced morphological transitions in linear BCP films have been observed in simulations and experiment, ^{63,72} we are not aware of any simulation or experimental work, to the best of our knowledge, predicting the same for MSP films.

Additional information can be gleaned by calculating the density of the blocks and solvent in the direction normal to the substrate. Figure 4 illustrates the number density profile of LSB beads calculated using eq 2 as the function of the distance along the direction normal to the substrate (z-direction) at different time values in the duration of the simulations. The number density is defined as

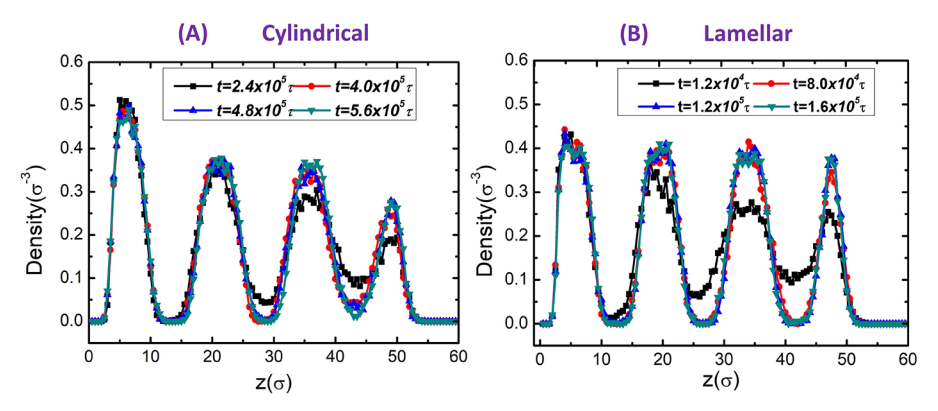


Figure 4. Low swelling block (LSB) number density profiles at different simulation times for ϵ_{12} = 0.75 (A) and ϵ_{12} = 1.10 (B) as a function of distance from the substrate.

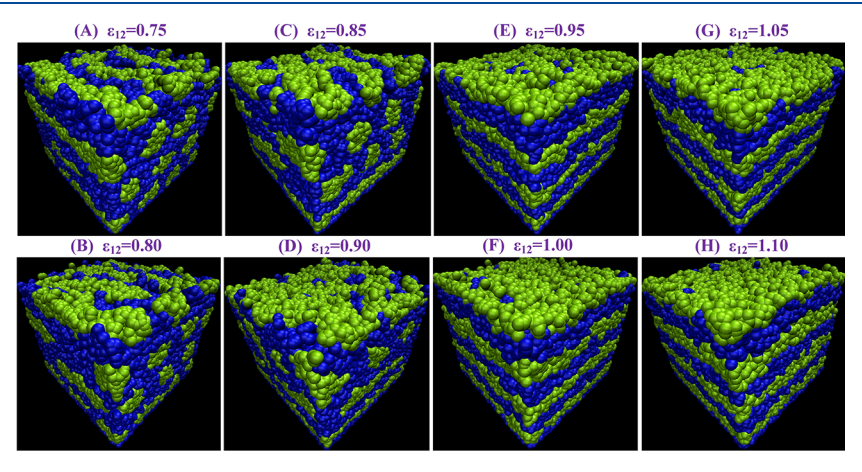


Figure 5. Final equilibrium morphology of MSP films: LSB (yellow) and HSB (blue) for different values of ϵ_{12} .

$$density = \frac{n_z}{V_z} \tag{2}$$

where, $n_z = \sum_i \delta(z - \mathbf{r}_i \cdot \hat{\mathbf{z}})$ is the number of beads (HSB, LSB) or SOL) in a given slab of thickness Δ at a distance z from the surface of the substrate. $V_z = L_x L_y \Delta$ is the volume of the slab with L_x and L_y the simulation box dimensions in the x- and ydirections, respectively. The effect of the substrate and the vapor in contact with the film play an important role in controlling the kinetics of the microphase separation process. While the density peaks close to the substrate attain their equilibrium value very fast, the density peaks close to the vapor phase take a much longer time to equilibrate especially for the cylindrical case (see Figure 4). The kinetics of equilibration for the cylindrical morphology is much slower and takes at least $t \approx 48 \times 10^4 \tau$ as shown in Figure 4A. On the other hand, the time evolution of the lamellar morphology is faster compared to cylindrical morphology and equilibrates within a short time of $t \approx 12 \times$ $10^4\tau$. This result is completely opposite to what we and others observed through simulation and experiment for the case of linear BCP thin films where it takes much longer time to form lamellar morphology than cylindrical morphology of linear BCP thin films in solution. From our earlier work, 63 the cylindrical morphology in linear thin BCP thin films equilibrated in a much shorter time of $t \approx 5 \times 10^3 \tau$ while the lamellar morphology equilibrated within $t \approx 12 \times 10^4 \tau$ which is similar to the MSP case (see Figure S3 in the SI). We thus conclude that the kinetics of equilibration of cylindrical morphology in MSP films is at least an order of magnitude slower than the kinetics of equilibration of cylindrical morphology in linear BCP films. Though it is computationally very expensive, it will be interesting to check in the future if this observation will hold true at higher molecular weights as well.

While the substrate is completely covered by the HSB beads for all cases, the composition of the layer of the film in contact with the vapor phase depends on the LSB-SOL interaction (ϵ_{12}) strength. The fraction of the LSB beads in that layer increases monotonically with increase in solvent quality, ϵ_{12} , and almost completely covers the layer at the highest good solvent condition we simulated, $\epsilon_{12} = 1.10$ (see Figure 5). The same result has been observed in our recent investigation of linear block copolymer films.⁶³ Furthermore, the thickness of the freesurface wetting layer is approximately half-lamellae thick which was also observed in direct solvent immersion annealing. Given that the LSB block has to completely wet the free surface in the absence of solvent since it has lower surface tension than the HSB block, the fractional distribution of the LSB block in the presence of solvent can be quantified following our recent approach using the following relative interaction parameter: 63

$$\beta_{ij} = \frac{\epsilon_{jj} - \epsilon_{ij}}{\epsilon_{jj}} \tag{3}$$

where j refers to block LSB or HSB and i represents solvent. The β_{ij} for all solvent interactions are tabulated in Table 2. When β_{ij} < 0, the solvent is a good solvent for that block. However, the relative value of β_{12} and β_{13} determines the fraction of the blocks in the topmost layer of the film and is completely covered by the

Table 2. Relative Interaction Parameter (β_{ij}) for Different Interaction Parameters (ϵ_{ii})

pairs (ij)	ϵ_{ij}	$oldsymbol{eta}_{ij}$
SOL-LSB(12)	0.75	0.17
SOL-LSB(12)	0.80	0.11
SOL-LSB(12)	0.85	0.06
SOL-LSB(12)	0.90	0.00
SOL-LSB(12)	0.95	-0.06
SOL-LSB(12)	1.00	-0.11
SOL-LSB(12)	1.05	-0.17
SOL-LSB(12)	1.1	-0.22
SOL-HSB(13)	1.2	-0.20

LSB block when $\beta_{12} < \beta_{13}$ which is the case for $\epsilon_{12} = 1.1$ (see Figure 5).

The morphology of the film away from the substrate and the free surface should be closer to its bulk morphology. Classically, the morphology of block copolymers is controlled by the volume fraction of the various blocks. In the present study, we have a symmetric MSP block copolymer and in the absence of solvent should form a lamellar morphology. The solvent thus plays the role of virtually changing the volume fraction of the two blocks. Two dimensional snapshots of equilibrated morphologies of MSP films (including solvent) for poor solvent and good solvent conditions are shown in Figure 6. From Figure 6 (poor solvent

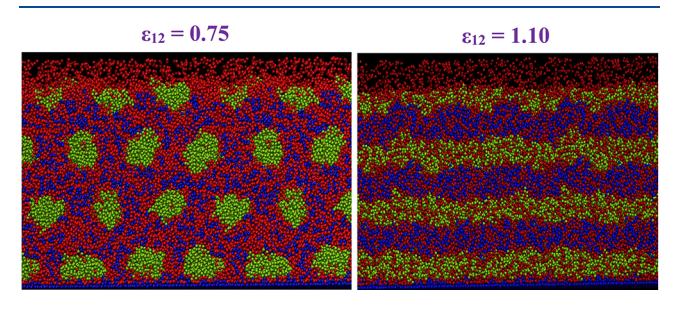


Figure 6. Final equilibrium morphology of the MSP films: LSB (yellow), HSB (blue) and SOL (red) for ϵ_{12} = 0.75 and ϵ_{12} = 1.10.

condition), it is clear that the solvent beads are abundant only within the regions occupied by HSB beads since they prefer to interact with themselves and HSB beads at these energetic conditions. Our observation is that for poor solvent condition, the volume fraction of HSB ($f_{\rm HSB}$) is dominant over that of LSB ($f_{\rm LSB}$), which leads to the cylindrical arrangement of LSB beads as shown in Figure 5. Furthermore, the quantitative description of the volume fraction can be explained using eq 4

$$f_{j} = \frac{V_{j} + V_{\text{SOL}-j}}{V_{\text{total}}} \tag{4}$$

where, j is either LSB or HSB, V_j is the volume of block j (LSB or HSB), $V_{\mathrm{SOL}-j}$ is the volume of solvent retained in block j and V_{total} is the total volume ($V_{\mathrm{LSB}}+V_{\mathrm{HSB}}+V_{\mathrm{SOL}}$). From visual inspection of Figure 6 (top panel) almost all the solvent is retained in the HSB domain, unlike LSB domain containing nearly no solvent. This ends up with the volume fraction of LSB and HSB to be $f_{\mathrm{LSB}}\approx 0.25$ and $f_{\mathrm{HSB}}\approx 0.75$, respectively. This value of f_{LSB} has been predicted theoretically for the cylindrical morphology of block copolymer films.

The alignment of cylindrical LSB rods can be determined by lower surface energy of LSB, preferential wetting of HSB on the substrate and limited film size. This phenomena is in agreement with the experimental findings where the preferential alignment of cylindrical and lamellar morphologies can be driven by substrate and free interface interactions. 86,87 From Figure 6, it is apparently evident that at smaller value of ϵ_{12} (poor solvent) almost no solvent is contained within the domain of LSB; on the other hand for good solvent condition the solvent beads are uniformly distributed throughout the film resulting in lamellar morphology. The other clear observation from Figure 6 (left panel) is that the first layers of LSB cylinders near the substrate are compressed in the lateral direction compared to those far from the substrate. For ϵ_{12} = 0.85 (i.e., increased solvent quality but still poor solvent condition) the first layer of cylinders have been connected to each other along the xy-plane of the surface becoming a single lamellar layer (see Figure 3A). This can be attributed to the compression of the cylinders in the lateral direction and the increase of solvent fraction in the LSB domain due to the increase in solvent quality.

To get a better understanding of the distribution of solvent in the LSB and HSB domains, the number density profile of the different types of beads (SOL, HSB, and LSB) at different values of ϵ_{12} is computed using eq 2, and the results are shown in Figure 7. Two different kinds of density profiles are shown for the

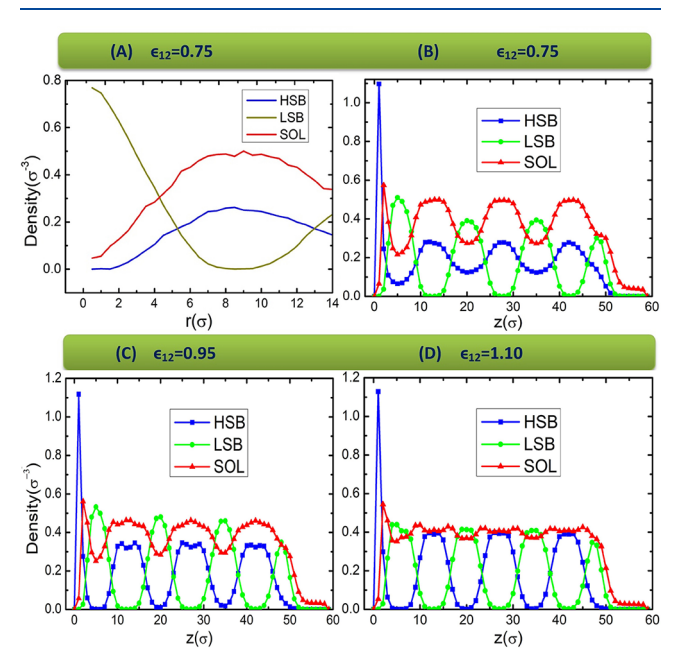


Figure 7. Number density profile of HSB, LSB, and SOL beads for different values of ϵ_{12} (see legends; A) as a function of distance from the principal axis of the LSB cylinders and (B–D) as a function of distance from the substrate surface.

cylindrical morphology cases ($\epsilon_{12}=0.75$) to clearly illustrate the distribution of the solvent in the blocks (Figure 7A) and also the distribution of the different beads with respect to the substrate (Figure 7B). A cylindrical coordinate system centered on the principal axis of each of the LSB cylinders was used for generating Figure 7A. In this particular case, r is the distance from the principal axis of each cylinder and a cylindrical shell of thickness Δ with shell volume of $V_r = \pi L_c \Delta (2r + \Delta)$ was used in determining the number density using eq 2, where L_c is the length of the cylinders. The density of solvent in the region of LSB domain is very small (Figure 7A), which results in cylindrical morphology but is uniformly distributed through out the film at $\epsilon_{12}=1.10$ (Figure 7D), resulting in lamellar

morphology. Though both LSB and HSB blocks are swollen by the solvent at ϵ_{12} = 0.95, the HSB domain is more swollen, by about 30%, resulting in asymmetric domain size in the lamellar morphology.

The number density profiles with respect to the substrate surface (Figure 7B,D) display several interesting features. The HSB layer near the substrate for all cases is characterized by a solvent-free HSB monolayer adjacent to a swollen HSB domain due to the fact that the substrate is highly selective to the HSB block but repulsive to solvent and LSB block. Above this first layer, ordered patterns of alternating domains, which are preferably filled by beads of the same type, emerge. Information about domain size and interfacial width can be directly determined from these ordered patterns for the case of lamellar morphology (good solvent conditions) and is discussed later in this section. Furthermore, from Figure 7, the density profile of the solvent shows several interesting behaviors: (1) relatively low solvent density is observed in the LSB domain for ϵ_{12} < 1.10, (2) almost uniform solvent density distribution for $\epsilon_{12} = 1.10$, but (3) slightly higher solvent density at the interface of HSB and LSB domains for ϵ_{12} = 1.10 to minimize the repulsion between LSB and HSB blocks at the interface. Our third observation is further validated by comparing the solvent density in the different domains from three independent runs and is shown in Figure S4 of the SI. Interestingly, we also observe a similar behavior in linear BCP films as also shown in the same

The density profiles as a function of the distance from the substrate (Figure 7B,D) are informative in explaining how the phase transition from cylindrical to lamellar morphology takes place as the solvent quality changes from poor to good condition. The z distance values at which LSB density profiles attain their respective peaks for cylindrical morphology (Figure 7B) are also the location of the middle of the LSB domains in the lamellar morphology. For instance, LSB distribution peaks are observed at $z \approx 5\sigma$, 20σ , 35σ , and 50σ for the cylindrical morphologies, shown in Figure 7B, which also correspond to the locations of the middle of the LSB domains in Figure 7C,D. Our observation is that as the quality of solvent increases, the cylindrical morphologies at those peak locations deform into elliptic cylinders with their larger radius parallel to the substrate and finally evolves to a lamellar morphology in a good solvent.

As discussed above, morphological transition from cylindrical to lamellar as the result of change in quality of solvent has been observed. In addition to transitions from one domain shape to the other, there seems to be change in the size (layer thickness in lamella and diameter in cylinder) of the domain shapes as the functions of solvent quality (ϵ_{12}). The domain size was calculated from their number density and by using ImageJ software. The time evolution of the domain size and its variation with solvent quality are shown in Figure 8. In order to see the effect of molecular architecture on the domain size, we recalculated the sizes of cylindrical and lamellar domains of the linear BCP thin films reported in our previous work and compared them with those of MSP thin films.

In Figure 8A, we plotted ensemble average size (denoted as R in units of σ) of lamella and cylinders of the LSB domains for $\epsilon_{12}=1.10$ and $\epsilon_{12}=0.75$ from three independent runs. From the figure, it is clearly evident that the thickness of the LSB domains in the lamellar morphology and the diameter of the LSB domains in the cylindrical morphology initially decreased with time before a steady-state value was reached about $t\approx 12\times 10^4\tau$ and $48\times 10^4\tau$ for lamellar and cylindrical morphologies,

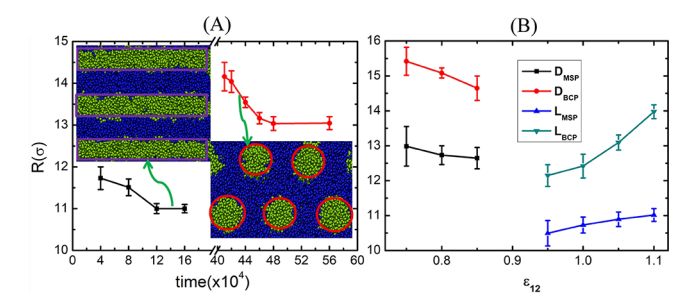


Figure 8. (A) Time evolution of LSB domain size (diameter for cylinder morphology and domain thickness for lamellar morphology) and (B) comparison between the domain sizes in linear BCP and MSP thin films as a function of ϵ_{12} where $D_{\rm MSP}$ and $D_{\rm BCP}$ refer to cylinder diameter in MSP and linear BCP films, respectively, and $L_{\rm MSP}$ and $L_{\rm BCP}$ refer to LSB lamellar domain size in MSP and linear BCP films, respectively. The error bars in (A) were generated from three independent runs while the error bars in (B) were generated from block average with $8\times 10^3 \tau$ block time interval.

respectively. As pointed out earlier, based on Figure 4, the cylindrical morphology took much longer time than the lamellar morphology to reach to a steady state. The steady state values of the thickness or diameter of the LSB domains as a function of solvent quality (ϵ_{12}) are shown in Figure 8B for both MSP and BCP thin films. From this figure, two simple and clear information can be grabbed. First, after transitioning from cylindrical to lamellar morphology at ϵ_{12} = 0.9 (which is a neutral solvent condition), the thickness of the LSB domains increases with increase in solvent quality. Second, the LSB domain sizes for MSP thin films are smaller than that of BCP thin films of same molecular weight. This makes the MSP films more attractive for achieving smaller domain sizes than their linear BCP counterparts.

In addition to analyzing domain sizes, it is also essential to reveal how the variation of solvent quality affects the state of individual chains. Sample snapshots of MSP thin films in poor solvent and good solvent conditions with magnified individual chains in different domain regions are shown in Figure 9. Several

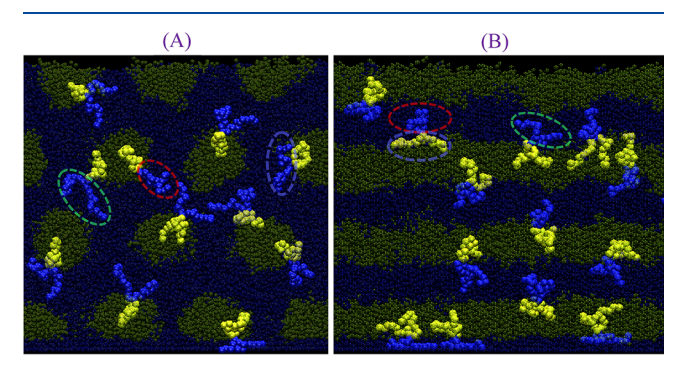


Figure 9. Representative snapshots with some of the chain magnified to show the conformation of the chains in the cylindrical (A) and lamellar (B) morphology.

different chain confirmations, including stretching and folding are observed in both cylindrical and lamellar morphologies similar to what we observed in linear BCP thin films. ⁶³

While loop and bridge chain conformations have been observed in miktoarms with diblock arms 89 and also triblock copolymers, 90 we only observe loop conformations for the type of miktoarms studied here (see Figure 1). Furthermore, several studies $^{91-93}$ have shown that changing the sequence on the

monomer length scale (such as tapers) instead of abrupt changes at the block junctions affects the chain conformation significantly. Therefore, in the future, it will be interesting to investigate the effect of tapers in the chain conformation and dynamics of miktoarm copolymers.

More detailed information about chain conformation can be extracted from the dependence of the radius of gyration of the chains and the stretching of the arms of the miktoarm chains on quality of solvent. The squared end-to-center distance (r^2) of the LSB and HSB arms with respect to the central bid of a miktoarm chain and the squared radius of gyration $(R_{\rm g}^{\ 2})$ of a miktoarm chain for all chains were computed in poor and good solvent conditions. Chains adsorbed to the substrate were excluded in both r^2 and $R_{\rm g}^{\ 2}$ calculations since they show a different structure and dynamics than the rest of the chains in the film. The number-averaged $R_{\rm g}^{\ 2}$ as a function of time (starting from $t=0\tau$) for different solvent quality is shown in Figure 10A. For all

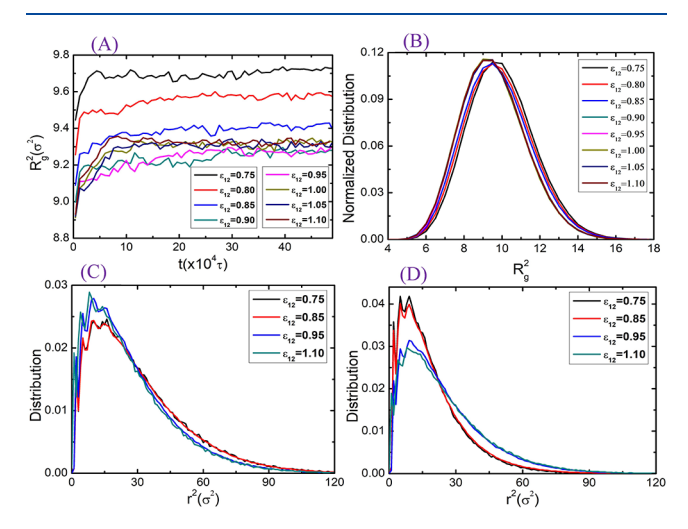


Figure 10. (A) Radius of gyration as a function of time starting from $t=0\tau$ for different solvent quality conditions. (B) The probability distribution of radius of gyration for different solvent quality conditions. Note that the distribution curves overlap for $\epsilon \geq 0.9$ (all good solvent conditions). Panels C and D are probability distribution of the squared end-to-center distance of the HSB and LSB arms, respectively, for different solvent quality conditions.

solvent conditions, the figure shows that the $R_{\rm g}^2$ values converge to their asymptotic values within $10^5\tau$ and the chains are slightly stretched in poor solvent (cylindrical morphology) conditions than in good solvent (lamellar morphology) conditions. The $R_{\rm g}^2$

distributions shown in Figure 10B clearly show two separated distributions where the distributions for poor solvent conditions are shifted toward larger $R_{\rm g}^2$ values. Furthermore, the r^2 distributions shown in Figure 10C (for HSB arms) and Figure 10D (for LSB arms) confirm that the stretching of the chains in cylindrical morphology is due to the stretching of the HSB arms that are apparently in the majority phase due to swelling by the solvent.

The three eigenvalues of the $R_{\rm g}^{\ 2}$ tensor shown in Figure S5 of the SI as a function of time further indicate that the chains are in a highly anisotropic conformation in both poor and good solvent conditions. To get a deeper insight into the conformation of the chains, we computed the squared end-to-end distance distribution between the end beads of the four arms resulting in three different types of distributions as depicted in Figure S6: (1) between LSB arms $(r_{LSB,LSB}^2)$, (2) between HSB arms $(r_{HSB,HSB}^2)$, and between LSB and HSB arms $(r_{LSB,HSB}^2)$. It is clear from the figure that the average distance between end beads of identical arms (Figure 11A and 11B) is smaller than the average distance between end beads of nonidentical arms (Figure 11C) resulting in the highly anisotropic conformation of the chains. Furthermore, average $r_{LSB,LSB}^2$ (Figure 11A) is smaller than average $r_{\text{HSB,HSB}}^2$ (Figure 11B) in poor solvent condition (cylindrical morphology) implying that the LSB arms in the cylinder domain are packed close to each other while the HSB arms in the majority domain are relatively spread out. When put together, the large width observed in the distribution of the R_g^2 and in all the different types of end-to-end distance distributions confirm the possibility of having different kinds of chain conformations in the form of stretching and folding across the interfaces as shown in Figure 9. The chains adsorbed on the substrate show a limited number of conformations since the HSB blocks lie completely flat on the substrate.

We have demonstrated that by varying solvent quality the morphology of MSP films can be controlled. Transitions from one morphological state to the other are the cumulative results of molecular scale reordering of each block of polymer chains and the effect of confining wall. Furthermore, distribution of chain end and central beads of the polymer chains could be affected by the variation of quality of solvent. We have analyzed the distribution of central beads as a function of distance from the substrate along the z-direction for good solvent condition and as the function of distance from the principal axis of the cylinders for poor solvent condition. We expect the central beads to be highly populated at the HSB-LSB interfaces for all cases. It is unlikely to find large population of central beads within a

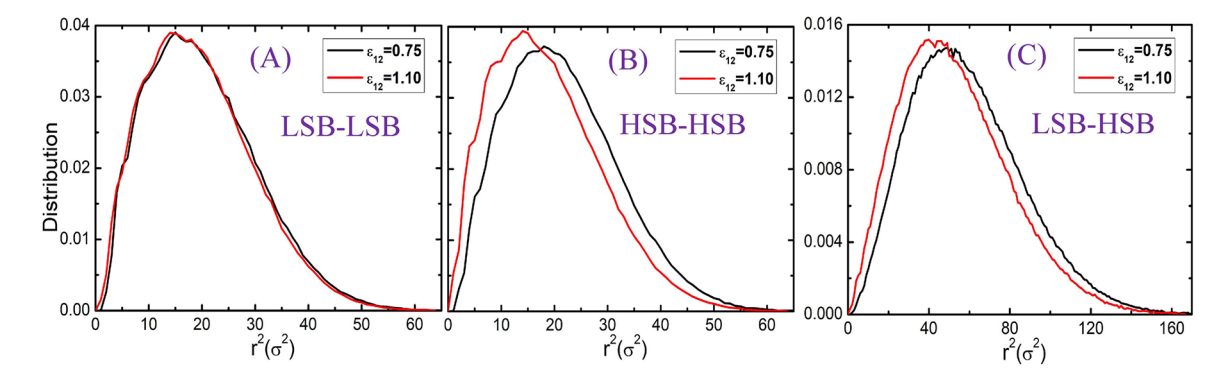


Figure 11. Distribution of the squared end-to-end distance between the end beads of (A) the two LSB arms, (B) the two HSB arms, and (C) between the LSB and HSB arms.

cylinder or within a lamellae as it violates the repulsive nature of interaction between HSB and LSB beads. This is visually verified in top row of Figure 12 where the magenta colored beads are the

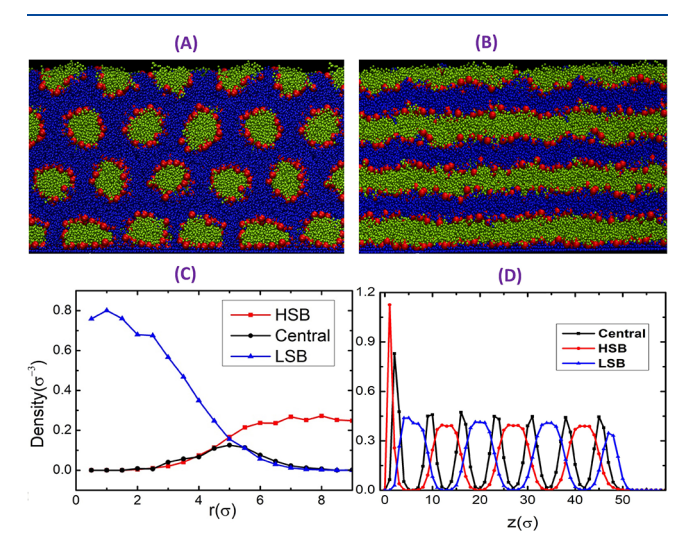


Figure 12. Panels A and B are snapshots showing the distribution of central beads with magenta color in cylindrical and lamellar morphology, respectively. Panels C and D are the number density profiles of HSB, LSB and central beads as a function of distance from the principal axis of the LSB cylinders in poor solvent condition ($\epsilon_{12} = 0.75$) and as a function of distance from the surface of the substrate located at z = 0 in good solvent condition ($\epsilon_{12} = 1.10$), respectively. The actual number density of central beads for both lamellar and cylindrical distributions are multiplied by 20 and 5, respectively, to make them appear on the same scale of HSB and LSB densities.

central beads. Also the bottom row of Figure 12 displays the density distribution profile of HSB, LSB, and central beads versus the radial distance from the center of cylinder (Figure 12C) and vertical distance from the substrate (Figure 12D). As hypothesized above, the density of the central beads is nonzero only at the HSB-LSB interfaces.

Furthermore, a very interesting behavior can be observed from the radial distribution function, g(r), of the central beads for different solvent quality conditions as shown in Figure 13A. The g(r) of the central beads exhibit similar behavior for all solvent quality conditions with same first peak location indicating that the location of the nearest neighbor central beads is the same in all morphologies. There is, however, a decrease in the height of the first peak of g(r) as the quality of solvent increases, an indication of a decrease in short-range

order due to more and more solvent diffusing into the LSB domain, and the location of the second and third nearest neighbors are moved to a lesser value for the case of good solvent conditions that result in lamellar morphology.

The temporal evolution of g(r) shown in Figure 13B,C for poor solvent and good solvent conditions, respectively, shows very interesting features. In both poor and good solvent conditions, the g(r) shows an ordered structure within a short time scale of $\sim 10^4 \tau$, then the peak of the first nearest neighbor increases with time, and also the location of the second and third peaks slowly shift to the right with time. The locations of the g(r) peaks in poor solvent condition and in early times actually overlap with the final locations of the g(r) peaks in good solvent condition (see Figure S7 in the SI). This seems to indicate that the central beads quickly rearrange in positions that are much faster to form lamellar morphology than cylindrical morphology as confirmed earlier.

However, close inspection of the g(r) in both poor and good solvent conditions indicate that the central beads g(r) is already equilibrated at a much earlier time than the $48 \times 10^4 \tau$ and $12 \times 10^4 \tau$ $10^4 \tau$ needed to form an equilibrated morphology in poor and good solvent conditions, respectively, inferred from the density plot shown in Figure 4. The g(r) results clearly tell us that most of the time is spent in rearranging the blocks in their respective domains once the central beads are very close to their equilibrium position (see the small change in g(r) between 12 $\times 10^4 \tau$ and $48 \times 10^4 \tau$ in poor solvent condition and between 3.2 $\times 10^4 \tau$ and $12 \times 10^4 \tau$ in good solvent conditions. Also confirmed by the two additional simulations done for each of the two cases). The g(r) results for the linear BCP cases shown in Figure S8 of the SI also agree with this last observation and clearly shows that the cylindrical morphology equilibrates much faster than all the other cases.

Though the change in morphology from cylindrical to lamellar and vice versa is significant, the g(r) results indicate that the central beads do not need to make significant readjustments in their packing during the transition of the polymer film from one morphology to another.

In order to gain further insight into the kinetics of morphological formation, we computed the mean-square displacement (MSD) of the center-of-mass of the chains during the early stages of morphological formation and also after a stable morphology is formed. The three orthogonal components of the MSD were calculated separately using the expression below:

$$MSD_{\alpha} = \langle [r_{i,\alpha}(t) - r_{i,\alpha}(0)]^2 \rangle$$
 (5)

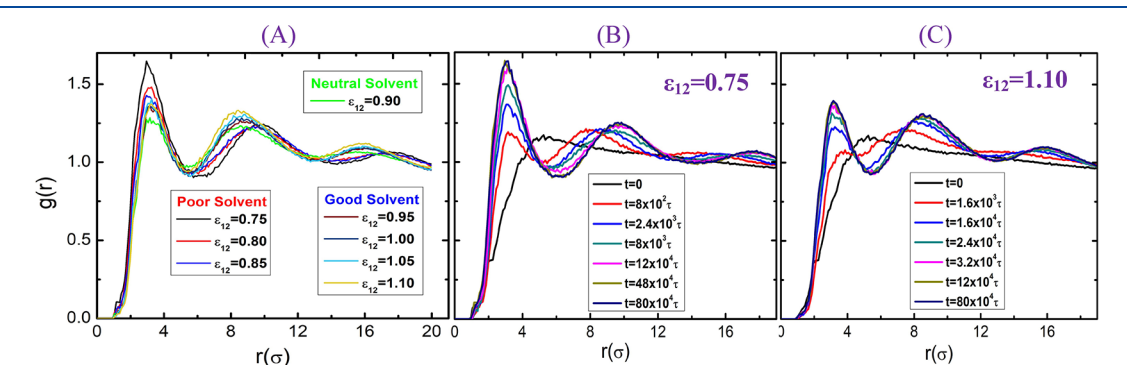


Figure 13. (A) Radial distribution of the central beads for different solvent quality conditions. (B and C) Temporal evolution of g(r) in poor and good solvent condition, respectively.

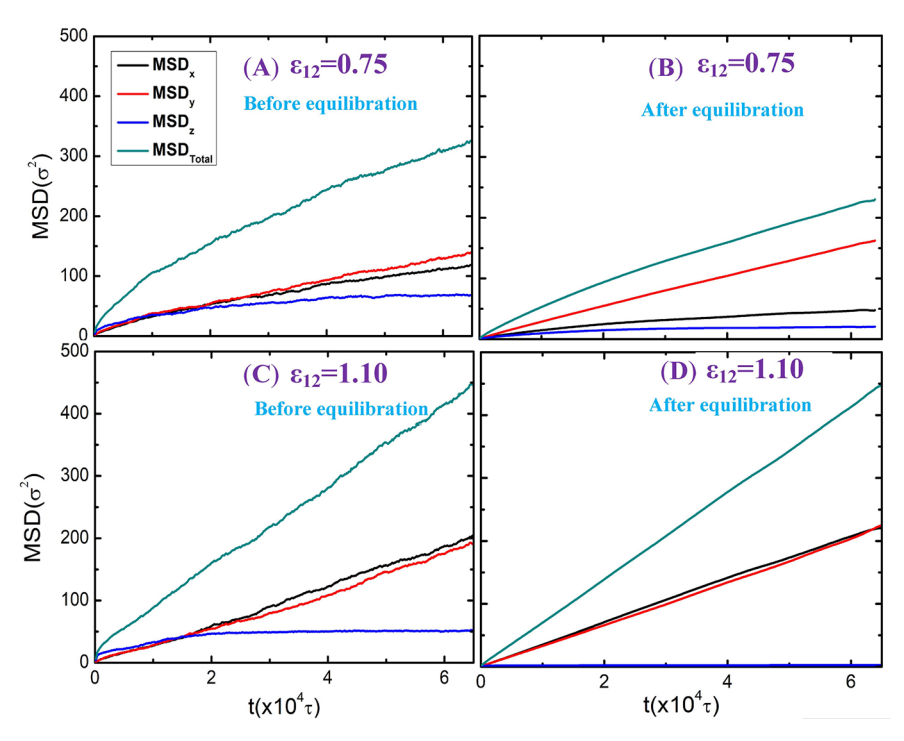


Figure 14. Panels A and C are nontime averaged mean-square displacements of the center-of-mass of MSP chains in poor and good solvent condition, respectively. Panels B and D are time-averaged mean-square displacements of the center-of-mass of MSP chains in poor and good solvent conditions, respectively. MSD_x, MSD_y, and MSD_z represent the components of the mean-square displacement in x-, y-, and z-direction, respectively.

I

where $\alpha = x, y,$ or $z, r_{i,\alpha}(t)$ is the α center-of-mass position of the ith chain at time t, and $\langle \cdots \rangle$ denotes the average for all chains. In time-averaged MSD calculations, usually computed after a system is equilibrated, $\langle \cdots \rangle$ also denotes average for all time origins available within the simulation.

Figure 14A,C shows the nontime-averaged MSD with respect to the position of the chains at $t = 0\tau$ in poor solvent and good solvent conditions, respectively. In both cases the dynamics in the perpendicular direction (MSD_z) quickly slows down while the dynamics in the parallel directions (MSD_x and MSD_y) show diffusive behavior. It is important to note that the principal axis of the cylindrical morphology, after it is stable, is in the ydirection and the lamellar morphology is in the parallel direction. Hence, the center-of-mass of the chains are already in their equilibrium z-position within a short time of $\sim 2 \times 10^4 \tau$ in good solvent condition (MSD, is constant beyond that time) while the chains in poor solvent condition are still moving in all directions. As already inferred from the g(r) data above, the MSD data also confirms that most of the chains quickly move into their morphological domain region, but then take comparatively long time for the blocks to pack and form a stable domain region. Once a stable morphology is formed, the chains motion is restricted within the domain as shown by the time-averaged MSD in Figure 14B for poor solvent condition (the motion of the chains is mostly constrained in the y-direction that is in the principal axis of the cylinders) and in Figure 14D for good solvent condition (the motion of the chains is constrained in the parallel direction with very little motion in the perpendicular direction).

CONCLUSIONS

The effects of solvent quality and substrate-block interactions on the morphological state of miktoarm star polymer (MSP) films were investigated by using coarse-grained molecular dynamics simulation of a bead-spring model. Varying the solvent-block relative interaction parameter significantly affected the morphology of the simulated systems. The spacial distribution of the solvent beads within the simulation box has also been highly influenced by those factors. In particular, in the present work, systematically changing the interaction strength between one block of the MSP and the solvent, while keeping the remaining different types of interaction parameters constant, resulted in a morphological transition from lamellar to cylindrical morphology for a system which is inherently lamellar in the absence of solvent. These morphological transitions are somehow directly linked to the unbalanced distribution of solvent beads throughout the film causing one block to behave like a minority phase and form a cylindrical morphology. The time taken to obtain a well ordered structure of the blocks into a cylindrical morphology was found to be much slower than the time taken to obtain ordered blocks into a lamellar morphology. In general, the simulated result showed that the kinetics of MSP thin film is much slower than that of linear block copolymer (BCP) thin films and the calculated sizes of LSB domains (diameters of cylinders in cylindrical morphology and thicknesses of lamellae in lamellar morphology) of MSP systems are significantly smaller than those of linear BCP of comparable molecular weight. It will be interesting, in future work, to examine the effect of evaporating the solvent on the final morphology of the MSP films studied in here.

The $(A_{10})_2$ –C– $(B_{10})_2$ MSP system investigated in detail in the present study could represent a wider range of polyphilic polymeric materials in which separate building blocks with different types of interaction sites are combined. Solvent and substrate induced submolecular partitioning and ordering enhancement in these materials create the opportunity to self-assemble into well-defined nanostructures for different potential applications. The coarse-grained simulation strategy presented here can be used as an inspiration toward further simulation and

experimental studies of MSP systems in a variety of substrates where different architectures and large system sizes of MSPs may offer a strong tool for the design of experiments.

ASSOCIATED CONTENT

Supporting Information

The Supporting Information is available free of charge at https://pubs.acs.org/doi/10.1021/acs.macromol.0c00770.

Computational details and additional results as discussed in the text (PDF)

AUTHOR INFORMATION

Corresponding Authors

Zerihun G. Workineh — Department of Materials Science, Bahir Dar University, Bahir Dar, Ethiopia; orcid.org/0000-0002-6191-7854; Email: workzer2005@gmail.com

Giuseppe Pellicane — Dipartimento di Scienze Biomediche, Odontoiatriche e delle Immagini Morfologiche e Funzionali, Università degli Studi di Messina, 98125 Messina, Italy; CNR-IPCF, 37-98158 Messina, Italy; School of Chemistry and Physics, University of Kwazulu-Natal, 3209 Pietermaritzburg, South Africa; Email: gpellicane@unime.it

Mesfin Tsige — Department of Polymer Science, University of Akron, Akron, Ohio, United States; ⊚ orcid.org/0000-0002-7540-2050; Email: mtsige@uakron.edu

Complete contact information is available at: https://pubs.acs.org/10.1021/acs.macromol.0c00770

Notes

The authors declare no competing financial interest.

ACKNOWLEDGMENTS

M.T. acknowledges financial support from the National Science Foundation (DMR-1912329). We would like to acknowledge the South African Center for High Performance (CHPC) and Dr A. Lopis for assistance and granting access to computational resources under the allocation MATS0887.

REFERENCES

- (1) Yan, D.; Zhou, Y.; Hou, J. Supramolecular self-assembly of macroscopic tubes. *Science* **2004**, *303*, 65–67.
- (2) Zhou, Y.; Huang, W.; Liu, J.; Zhu, X.; Yan, D. Self-assembly of hyperbranched polymers and its biomedical applications. *Adv. Mater.* **2010**, 22, 4567–4590.
- (3) Zhou, Y.; Yan, D. Supramolecular self-assembly of giant polymer vesicles with controlled sizes. *Angew. Chem., Int. Ed.* **2004**, 43, 4896–4899.
- (4) Hong, H.; Mai, Y.; Zhou, Y.; Yan, D.; Cui, J. Self-assembly of large multimolecular micelles from hyperbranched star copolymers. *Macromol. Rapid Commun.* **2007**, 28, 591–596.
- (5) Thota, B. N.; Urner, L. H.; Haag, R. Supramolecular architectures of dendritic amphiphiles in water. *Chem. Rev.* **2016**, *116*, 2079–2102.
- (6) Hermans, T. M.; Broeren, M. A.; Gomopoulos, N.; Van Der Schoot, P.; Van Genderen, M. H.; Sommerdijk, N. A.; Fytas, G.; Meijer, E. Self-assembly of soft nanoparticles with tunable patchiness. *Nat. Nanotechnol.* **2009**, *4*, 721.
- (7) Wu, W.; Wang, W.; Li, J. Star polymers: Advances in biomedical applications. *Prog. Polym. Sci.* **2015**, *46*, 55–85.
- (8) Huan, X.; Wang, D.; Dong, R.; Tu, C.; Zhu, B.; Yan, D.; Zhu, X. Supramolecular ABC miktoarm star terpolymer based on host–guest inclusion complexation. *Macromolecules* **2012**, *45*, 5941–5947.
- (9) Gou, P.-F.; Zhu, W.-P.; Shen, Z.-Q. Synthesis, self-assembly, and drug-loading capacity of well-defined cyclodextrin-centered drug-conjugated amphiphilic A14B7 miktoarm star copolymers based on

- poly (ε -caprolactone) and poly (ethylene glycol). *Biomacromolecules* **2010**, 11, 934–943.
- (10) Soliman, G. M.; Sharma, A.; Maysinger, D.; Kakkar, A. Dendrimers and miktoarm polymers based multivalent nanocarriers for efficient and targeted drug delivery. *Chem. Commun.* **2011**, *47*, 9572–9587.
- (11) Diep, J.; Tek, A.; Thompson, L.; Frommer, J.; Wang, R.; Piunova, V.; Sly, J.; La, Y.-H. Layer-by-layer assembled core—shell star block copolymers for fouling resistant water purification membranes. *Polymer* **2016**, *103*, 468–477.
- (12) Tekinalp, O.; Alsoy Altinkaya, S. Development of high flux nanofiltration membranes through single bilayer polyethyleneimine/alginate deposition. *J. Colloid Interface Sci.* **2019**, 537, 215–227.
- (13) Broz, P.; Driamov, S.; Ziegler, J.; Ben-Haim, N.; Marsch, S.; Meier, W.; Hunziker, P. Toward intelligent nanosize bioreactors: a pH-switchable, channel-equipped, functional polymer nanocontainer. *Nano Lett.* **2006**, *6*, 2349–2353.
- (14) Ranquin, A.; Versées, W.; Meier, W.; Steyaert, J.; Van Gelder, P. Therapeutic nanoreactors: combining chemistry and biology in a novel triblock copolymer drug delivery system. *Nano Lett.* **2005**, *5*, 2220–2224.
- (15) Soleyman, R.; Hirbod, S.; Adeli, M. Advances in the biomedical application of polymer-functionalized carbon nanotubes. *Biomater. Sci.* **2015**, *3*, 695–711.
- (16) Fukukawa, K.-i.; Rossin, R.; Hagooly, A.; Pressly, E. D.; Hunt, J. N.; Messmore, B. W.; Hawker, C. J. Synthesis and Characterization of Core—Shell Star Copolymers for In Vivo PET Imaging Applications. *Biomacromolecules* **2008**, *9*, 1329—1339.
- (17) Wang, Y.; Hong, C.-Y.; Pan, C.-Y. Spiropyran-Based Hyperbranched Star Copolymer: Synthesis, Phototropy, FRET, and Bioapplication. *Biomacromolecules* **2012**, *13*, 2585–2593.
- (18) Elabd, Y. A.; Hickner, M. A. Block copolymers for fuel cells. *Macromolecules* **2011**, 44, 1–11.
- (19) Bates, C. M.; Bates, F. S. 50th Anniversary Perspective: Block Polymers—Pure Potential. *Macromolecules* **2017**, *50*, 3–22.
- (20) Young, W.-S.; Kuan, W.-F.; Epps, T. H., III Block copolymer electrolytes for rechargeable lithium batteries. *J. Polym. Sci., Part B: Polym. Phys.* **2014**, *52*, 1–16.
- (21) Sanders, D. P. Advances in patterning materials for 193 nm immersion lithography. *Chem. Rev.* **2010**, *110*, 321–360.
- (22) Samant, S. P.; Grabowski, C. A.; Kisslinger, K.; Yager, K. G.; Yuan, G.; Satija, S. K.; Durstock, M. F.; Raghavan, D.; Karim, A. Directed self-assembly of block copolymers for high breakdown strength polymer film capacitors. *ACS Appl. Mater. Interfaces* **2016**, 8, 7966–7976.
- (23) Khanna, K.; Varshney, S.; Kakkar, A. Miktoarm star polymers: advances in synthesis, self-assembly, and applications. *Polym. Chem.* **2010**, *1*, 1171–1185.
- (24) Moughton, A. O.; Hillmyer, M. A.; Lodge, T. P. Multicompartment block polymer micelles. *Macromolecules* **2012**, *45*, 2–19.
- (25) Li, Z.; Kesselman, E.; Talmon, Y.; Hillmyer, M. A.; Lodge, T. P. Multicompartment micelles from ABC miktoarm stars in water. *Science* **2004**, *306*, 98–101.
- (26) Schacher, F. H.; Rupar, P. A.; Manners, I. Functional block copolymers: nanostructured materials with emerging applications. *Angew. Chem., Int. Ed.* **2012**, *51*, 7898–7921.
- (27) Li, Z.; Hillmyer, M. A.; Lodge, T. P. Morphologies of multicompartment micelles formed by ABC miktoarm star terpolymers. *Langmuir* **2006**, *22*, 9409–9417.
- (28) Saito, N.; Liu, C.; Lodge, T. P.; Hillmyer, M. A. Multicompartment micelle morphology evolution in degradable miktoarm star terpolymers. *ACS Nano* **2010**, *4*, 1907–1912.
- (29) Walther, A.; Müller, A. H. Janus particles. Soft Matter 2008, 4, 663–668
- (30) Erhardt, R.; Böker, A.; Zettl, H.; Kaya, H.; Pyckhout-Hintzen, W.; Krausch, G.; Abetz, V.; Müller, A. H. Janus micelles. *Macromolecules* **2001**, *34*, 1069–1075.

- (31) Walther, A.; Muller, A. H. Janus particles: synthesis, self-assembly, physical properties, and applications. *Chem. Rev.* **2013**, *113*, 5194–5261.
- (32) Liu, Y.; Abetz, V.; Müller, A. H. Janus cylinders. *Macromolecules* **2003**, *36*, 7894–7898.
- (33) Walther, A.; André, X.; Drechsler, M.; Abetz, V.; Müller, A. H. Janus discs. J. Am. Chem. Soc. 2007, 129, 6187–6198.
- (34) Groschel, A. H.; Schacher, F. H.; Schmalz, H.; Borisov, O. V.; Zhulina, E. B.; Walther, A.; Muller, A. H.E. Precise hierarchical self-assembly of multicompartment micelles. *Nat. Commun.* **2012**, *3*, 710.
- (35) Tsitsilianis, C.; Papanagopoulos, D.; Lutz, P. Amphiphilic heteroarm star copolymers of polystyrene and poly (ethylene oxide). *Polymer* **1995**, *36*, *3745*–*3752*.
- (36) Pispas, S.; Hadjichristidis, N.; Potemkin, I.; Khokhlov, A. Effect of architecture on the micellization properties of block copolymers: A2B miktoarm stars vs AB diblocks. *Macromolecules* **2000**, 33, 1741–1746.
- (37) Voulgaris, D.; Tsitsilianis, C.; Esselink, F.; Hadziioannou, G. Polystyrene/poly (2-vinyl pyridine) heteroarm star copolymer micelles in toluene: morphology and thermodynamics. *Polymer* **1998**, *39*, 6429–6439.
- (38) Li, B.; Zhao, L.; Qian, H.-J.; Lu, Z.-Y. Coarse-grained simulation study on the self-assembly of miktoarm star-like block copolymers in various solvent conditions. *Soft Matter* **2014**, *10*, 2245–2252.
- (39) Havránková, J.; Limpouchová, Z.; Štěpánek, M.; Procházka, K. Self-Assembly of Heteroarm Star Copolymers—A Monte Carlo Study. *Macromol. Theory Simul.* **2007**, *16*, 386—398.
- (40) Chang, Y.; Chen, W.-C.; Sheng, Y.-J.; Jiang, S.; Tsao, H.-K. Intramolecular janus segregation of a heteroarm star copolymer. *Macromolecules* **2005**, 38, 6201–6209.
- (41) Bačová, P.; Rissanou, A. N.; Harmandaris, V. Modelling of novel polymer materials through atomistic molecular dynamics simulations. *Procedia Computer Science* **2018**, *136*, 341–350.
- (42) Song, X.; Zhao, S.; Fang, S.; Ma, Y.; Duan, M. Mesoscopic simulations of adsorption and association of PEO-PPO-PEO triblock copolymers on a hydrophobic surface: From mushroom hemisphere to rectangle brush. *Langmuir* **2016**, 32, 11375–11385.
- (43) Tan, H.; Wang, W.; Yu, C.; Zhou, Y.; Lu, Z.; Yan, D. Dissipative particle dynamics simulation study on self-assembly of amphiphilic hyperbranched multiarm copolymers with different degrees of branching. *Soft Matter* **2015**, *11*, 8460–8470.
- (44) Lodge, T. P.; Pudil, B.; Hanley, K. J. The full phase behavior for block copolymers in solvents of varying selectivity. *Macromolecules* **2002**, *35*, 4707–4717.
- (45) Hanley, K. J.; Lodge, T. P. Effect of dilution on a block copolymer in the complex phase window. *J. Polym. Sci., Part B: Polym. Phys.* **1998**, 36, 3101–3113.
- (46) Abetz, V.; Simon, P. F. Block copolymers I; Springer, 2005; pp 125–212.
- (47) Suo, T.; Yan, D.; Yang, S.; Shi, A.-C. A theoretical study of phase behaviors for diblock copolymers in selective solvents. *Macromolecules* **2009**, 42, 6791–6798.
- (48) Wołoszczuk, S.; Banaszak, M.; Knychała, P.; Radosz, M. Monte Carlo phase diagram of symmetric diblock copolymer in selective solvent. *Macromolecules* **2008**, *41*, 5945–5951.
- (49) Levine, W. G.; Seo, Y.; Brown, J. R.; Hall, L. M. Effect of sequence dispersity on morphology of tapered diblock copolymers from molecular dynamics simulations. *J. Chem. Phys.* **2016**, *145*, 234907.
- (50) Darling, S. Directing the self-assembly of block copolymers. *Prog. Polym. Sci.* **2007**, 32, 1152–1204.
- (51) Bates, F. S.; Fredrickson, G. H. Block copolymer thermodynamics: theory and experiment. *Annu. Rev. Phys. Chem.* **1990**, 41, 525–557.
- (52) Paradiso, S. P.; Delaney, K. T.; García-Cervera, C. J.; Ceniceros, H. D.; Fredrickson, G. H. Block copolymer self assembly during rapid solvent evaporation: insights into cylinder growth and stability. *ACS Macro Lett.* **2014**, *3*, 16–20.

- (53) Sinturel, C.; Vayer, M.; Morris, M.; Hillmyer, M. A. Solvent vapor annealing of block polymer thin films. *Macromolecules* **2013**, *46*, 5399–5415.
- (54) Jeong, S.-J.; Kim, J. Y.; Kim, B. H.; Moon, H.-S.; Kim, S. O. Directed self-assembly of block copolymers for next generation nanolithography. *Mater. Today* **2013**, *16*, 468–476.
- (55) Albert, J. N.; Epps, T. H., III Self-assembly of block copolymer thin films. *Mater. Today* **2010**, *13*, 24–33.
- (56) Jung, Y. S.; Ross, C. A. Solvent-Vapor-Induced Tunability of Self-Assembled Block Copolymer Patterns. *Adv. Mater.* **2009**, *21*, 2540–2545
- (57) Ji, S.; Wan, L.; Liu, C.-C.; Nealey, P. F. Directed self-assembly of block copolymers on chemical patterns: A platform for nanofabrication. *Prog. Polym. Sci.* **2016**, *54*, 76–127.
- (58) Posel, Z.; Posocco, P.; Fermeglia, M.; Lísal, M.; Pricl, S. Modeling hierarchically structured nanoparticle/diblock copolymer systems. *Soft Matter* **2013**, *9*, 2936–2946.
- (59) Barandiaran, I.; Kortaberria, G. Selective placement of magnetic Fe3O4 nanoparticles into the lamellar nanostructure of PS-b-PMMA diblock copolymer. *Eur. Polym. J.* **2015**, *68*, 57–67.
- (60) Wood, D. S.; Koutsos, V.; Camp, P. J. Computer simulations of surface deposition of amphiphilic diblock copolymers driven by solvent evaporation. *Soft Matter* **2013**, *9*, 3758–3766.
- (61) Longanecker, M.; Modi, A.; Dobrynin, A.; Kim, S.; Yuan, G.; Jones, R.; Satija, S.; Bang, J.; Karim, A. Reduced Domain Size and Interfacial Width in Fast Ordering Nanofilled Block Copolymer Films by Direct Immersion Annealing. *Macromolecules* **2016**, *49*, 8563–8571.
- (62) Wang, Z.; Shao, J.; Pan, H.; Feng, X.; Chen, P.; Xia, R.; Wu, X.; Qian, J. Monte Carlo simulations of the phase separation of a copolymer blend in a thin film. *ChemPhysChem* **2015**, *16*, 567–571.
- (63) Modi, A.; Karim, A.; Tsige, M. Solvent and Substrate Induced Synergistic Ordering in Block Copolymer Thin Films. *Macromolecules* **2018**, *51*, 7186–7196.
- (64) Forrey, C.; Yager, K. G.; Broadaway, S. P. Molecular Dynamics Study of the Role of the Free Surface on Block Copolymer Thin Film Morphology and Alignment. *ACS Nano* **2011**, *5*, 2895–2907.
- (65) Yager, K. G.; Lai, E.; Black, C. T. Self-Assembled Phases of Block Copolymer Blend Thin Films. ACS Nano 2014, 8, 10582–10588.
- (66) Peters, B. L.; Pike, D. Q.; Rubinstein, M.; Grest, G. S. Polymers at Liquid/Vapor Interface. ACS Macro Lett. 2017, 6, 1191–1195.
- (67) Li, S.-J.; Qian, H.-J.; Lu, Z.-Y. A simulation study on the glass transition behavior and relevant segmental dynamics in free-standing polymer nanocomposite films. *Soft Matter* **2019**, *15*, 4476–4485.
- (68) Kravchenko, V. S.; Potemkin, I. I. Self-assembly of rarely polymer-grafted nanoparticles in dilute solutions and on a surface: From non-spherical vesicles to graphene-like sheets. *Polymer* **2018**, *142*, 23–32.
- (69) Modi, A.; Bhaway, S. M.; Vogt, B. D.; Douglas, J. F.; Al-Enizi, A.; Elzatahry, A.; Sharma, A.; Karim, A. Direct Immersion Annealing of Thin Block Copolymer Films. *ACS Appl. Mater. Interfaces* **2015**, 7, 21639–21645.
- (70) Park, W. I.; Kim, J. M.; Jeong, J. W.; Jung, Y. S. Deep-Nanoscale Pattern Engineering by Immersion-Induced Self-Assembly. *ACS Nano* **2014**, *8*, 10009–10018.
- (71) Samant, S. P.; Grabowski, C. A.; Kisslinger, K.; Yager, K. G.; Yuan, G.; Satija, S. K.; Durstock, M. F.; Raghavan, D.; Karim, A. Directed Self-Assembly of Block Copolymers for High Breakdown Strength Polymer Film Capacitors. *ACS Appl. Mater. Interfaces* **2016**, 8, 7966–7976.
- (72) Chavis, M. A.; Smilgies, D.-M.; Wiesner, U. B.; Ober, C. K. Widely Tunable Morphologies in Block Copolymer Thin Films Through Solvent Vapor Annealing Using Mixtures of Selective Solvents. *Adv. Funct. Mater.* **2015**, *25*, 3057–3065.
- (73) Cummins, C.; Morris, M. A. Using block copolymers as infiltration sites for development of future nanoelectronic devices: Achievements, barriers, and opportunities. *Microelectron. Eng.* **2018**, 195, 74–85.

- (74) Yang, Q.; Loos, K. Perpendicular Structure Formation of Block Copolymer Thin Films during Thermal Solvent Vapor Annealing: Solvent and Thickness Effects. *Polymers* **2017**, *9*.525
- (75) Jung, H.; Shin, W. H.; Park, T. W.; Choi, Y. J.; Yoon, Y. J.; Park, S. H.; Lim, J.-H.; Kwon, J.-D.; Lee, J. W.; Kwon, S.-H.; Seong, G. H.; Kim, K. H.; Park, W. I. Hierarchical multi-level block copolymer patterns by multiple self-assembly. *Nanoscale* **2019**, *11*, 8433–8441.
- (76) Kremer, K.; Grest, G. S. Dynamics of entangled linear polymer melts: A molecular-dynamics simulation. *J. Chem. Phys.* **1990**, 92, 5057–5086.
- (77) Dünweg, B.; Kremer, K. Microscopic verification of dynamic scaling in dilute polymer solutions: A molecular-dynamics simulation. *Phys. Rev. Lett.* **1991**, *66*, 2996–2999.
- (78) Gu, X.; Gunkel, I.; Hexemer, A.; Gu, W.; Russell, T. P. An in-situ grazing incidence X-Ray scattering study of block copolymer thin films during solvent vapor annealing. *Adv. Mater.* **2014**, *26*, 273–281.
- (79) Sinturel, C.; Vayer, M.; Morris, M.; Hillmyer, M. A. Solvent vapor annealing of block polymer thin films. *Macromolecules* **2013**, *46*, 5399–5415.
- (80) Tsige, M.; Grest, G. S. Molecular dynamics simulation of solvent-polymer interdiffusion: Fickian diffusion. *J. Chem. Phys.* **2004**, *120*, 2989–2995.
- (81) Plimpton, S.; Hendrickson, B. Parallel Computing in Computational Chemistry; Wiley, 2008; Chapter 9, pp 114–132.
- (82) Kim, B. H.; Lee, H. M.; Lee, J.-H.; Son, S.-W.; Jeong, S.-J.; Lee, S.; Lee, D. I.; Kwak, S. U.; Jeong, H.; Shin, H.; et al. Spontaneous Lamellar Alignment in Thickness-Modulated Block Copolymer Films. *Adv. Funct. Mater.* **2009**, *19*, 2584–2591.
- (83) Ruiz, R.; Bosworth, J.; Black, C. Effect of structural anisotropy on the coarsening kinetics of diblock copolymer striped patterns. *Phys. Rev. B: Condens. Matter Mater. Phys.* **2008**, *77*, 054204.
- (84) Fasolka, M. J.; Mayes, A. M. Block Copolymer Thin Films: Physics and Applications. *Annu. Rev. Mater. Res.* **2001**, *31*, 323–355.
- (85) Mai, Y.; Eisenberg, A. Self-assembly of block copolymers. *Chem. Soc. Rev.* **2012**, *41*, 5969–5985.
- (86) Albert, J. N.; Epps, T. H. Self-assembly of block copolymer thin films. *Mater. Today* **2010**, *13*, 24–33.
- (87) Han, E.; Stuen, K. O.; Leolukman, M.; Liu, C.-C.; Nealey, P. F.; Gopalan, P. Perpendicular Orientation of Domains in Cylinder-Forming Block Copolymer Thick Films by Controlled Interfacial Interactions. *Macromolecules* **2009**, *42*, 4896–4901.
- (88) Rueden, C. T.; Schindelin, J.; Hiner, M. C.; DeZonia, B. E.; Walter, A. E.; Arena, E. T.; Eliceiri, K. W. ImageJ2: ImageJ for the next generation of scientific image data. *BMC Bioinf.* **2017**, *18*, 529.
- (89) Spencer, R. K. W.; Matsen, M. W. Domain bridging in thermoplastic elastomers of star block copolymer. *Macromolecules* **2017**, *50*, 1681–1687.
- (90) Karatasos, K.; Anastasiadis, S. H.; Pakula, H.; Watanabe, H. On the loops-to-bridges ratio in ordered triblock copolymers: An investigation by dielectric relaxation spectroscopy and computer simulations. *Macromolecules* **2000**, *33*, 523–541.
- (91) Seo, Y.; Brown, J. R.; Hall, L. M. Effect of tapering on morphology and interfacial behavior of diblock copolymers from molecular dynamics simulations. *Macromolecules* **2015**, *48*, 4974–4982.
- (92) Kuan, W.; Roy, R.; Rong, L.; Hsiao, B. S.; Epps, T. H., III Design and synthesis of network-forming triblock copolymers using tapered block interfaces. *ACS Macro Lett.* **2012**, *1*, 519–523.
- (93) Patterson, A. L.; Danielsen, S. P. O.; Yu, B.; Davidson, E. C.; Fredrickson, G. H.; Segalman, R. A. Sequence Effects on block copolymer self-assembly through tuning chain conformation and segregation strength utilizing sequence-defined polypetoids. *Macromolecules* **2019**, *52*, 1277–1286.

■ NOTE ADDED AFTER ASAP PUBLICATION

This paper published ASAP on July 24, 2020 with errors in the Supporting Information file. A new file was uploaded and the paper was reposted on July 27, 2020.